A case study of using X-ray Thomson Scattering to diagnose the in-flight plasma conditions of DT cryogenic implosions

H. Poole[1],* D. Cao[2], R. Epstein[2], I. Golovkin[3], T. Walton[3], S. X. Hu[2,4], M. Kasim[1], S. M. Vinko[1,5], J. R. Rygg[2,4], V. N. Goncharov[2,4], G. Gregori[1], and S. P. Regan[2,4]
[1]*Department of Physics, University of Oxford, Oxford, OX1 3PU, UK*
[2]*Laboratory for Laser Energetics, University of Rochester, Rochester, New York 14623, USA*
[3]*Prism Computational Sciences, Madison, Wisconsin 53711, USA*
[4]*Department of Mechanical Engineering, University of Rochester, Rochester, New York 14611, USA and*
[5]*Central Laser Facility, STFC Rutherford Appleton Laboratory, Didcot, OX11 0QX, UK*
(Dated: May 30, 2022)

The design of inertial confinement fusion (ICF) ignition targets requires radiation-hydrodynamics simulations with accurate models of the fundamental material properties (i.e., equation of state, opacity, and conductivity). Validation of these models are required via experimentation. A feasibility study of using spatially-integrated, spectrally-resolved, X-ray Thomson scattering (XRTS) measurements to diagnose the temperature, density, and ionization of the compressed DT shell of a cryogenic DT implosion at two-thirds convergence was conducted. Synthetic scattering spectra were generated using 1-D implosion simulations from the LILAC code that were post processed with the X-ray Scattering (XRS) model which is incorporated within SPECT3D. Analysis of two extreme adiabat capsule conditions showed that the plasma conditions for both compressed DT shells could be resolved.

I. INTRODUCTION

The design of inertial confinement fusion (ICF) targets is a challenging task that requires, among others, hydrodynamic simulations with knowledge of the shocked materials' equation of state (EOS) if ignition conditions are to be achieved [1–5]. The theoretical modeling of the extreme matter properties reached during the capsule implosion is difficult due to the need of a quantum mechanical treatment of the degenerate electrons, moderate strongly-coupled ions and many-particle correlations [6–9]. Uncertainty in the EOS of matter under this regime results in unconfirmed calculations for transport properties, ionization balance, and energy and temperature equilibration [10–14]. Therefore, experimental validation is vital for benchmarking and developing reduced models that can be implemented in radiation hydrodynamic codes.

At present, the diagnosis of the physical properties of dense plasmas produced in ICF implosions is limited due to the difficulty in achieving the required accuracy and spatial resolutions [15–18] for different model predictions to be tested. Over the past couple of decades there has been a push to develop new diagnostics that may be able to resolve different regions of the imploding capsule. Multi-keV spectrally resolved x-ray Thomson scattering (XRTS) is one of these techniques [18–20]. Presented here is a methodology for resolving the in-flight compressed shell conditions.

The first experimental observation of noncollective, inelastic x-ray scattering from shocked liquid deuterium is discussed in Ref. [17]. This demonstrated the capabilities of inferring the electron temperature, ionization and electron density from the shapes and intensities of the elastic (Rayleigh) and inelastic (Compton) components in the scattering spectra in ICF dense matter. However, the scattering data had no spatial information, nor did the analysis performed provide the capability to separate the contribution from different regions.

Spatial temperature and ionization profiles were determined from a near-solid density foam using a collimated X-ray beam in Ref. [21]. This data, produced using the Imaging X-ray Thomson Spectrometer (IXTS) at the Omega laser facility [22, 23], determined the temperature and ionization state of the carbon foam at multiple positions along the axis of the flow. Good agreement was found between the experiment and theoretical predictions with the exception of the high-temperature, low-density rarefaction region of the blast wave.

Simultaneous collective and non-collective scattering data for dynamically compressed deuterium was collected in Ref. [24] using the 2 keV Si Ly-α line. This focused on compression states of $\rho/\rho_0 \sim 2.8 - 4.05$. The mass density was determined using the VISAR shock velocity using current EOS data. This allowed for a restriction on the parameter space when determining the ionization from the XRTS data.

To date, experiments have successfully been conducted at the Omega laser facility to determine conditions on spherical CH implosions in Refs. [25, 26]. However, no attempt has yet been made to field an XRTS diagnostic on a laser direct-drive ICF implosion of a layered, cryogenic deuterium-tritium (DT) spherical target. In this report the feasibility of utilizing spatially integrated XRTS measurements to determine the in-flight conditions of the compressed DT shell will be investigated. The study involved analyzing the X-ray scattering data produced by targets with very different adiabats. The adiabat is defined as the ratio of the plasma pressure to the Fermi-

* Corresponding author address: hannah.poole@physics.ox.ac.uk

degenerate pressure [27] and for DT fuel is given by [28]

$$\alpha_{DT} \simeq \frac{P_{\rm Shell}[\rm Mbar]}{2.2\,[\rho[\rm g/cm^3]]^{5/3}}\,. \quad (1)$$

Confinement properties of an ICF capsule depend on the areal density of the compressed shell and hot-spot, ρR. The areal density is controlled by varying the entropy of the fuel, which is determined by the fuel adiabat. For ignition to occur, a large enough areal density (low adiabat), $> 0.2 - 0.5\,\rm g/cm^2$, and hot enough core, $\sim 5 - 12\,\rm keV$, are required [29, 30]. However, targets imploded on a low adiabat are susceptible to hydrodynamic instabilities [31, 32] that drive the rapid growth of nonuniformities. Therefore, an important part of ICF research involves optimization of the adiabat [33–35]. In experiments, however, direct measurements of the in-flight fuel adiabat and densities are not yet achievable, instead they are inferred from the neutron yield and x-ray self-emission [36].

For this feasibility paper, the target chosen for the high adiabat design was used in the first phase of the performance optimization campaign (this campaign has since set the record neutron yield on OMEGA [37]) and is considered a good design reference point for a stable implosion. The lower adiabat target design used was part of a campaign to probe performance right below an observed 'stability cliff' [38] that is still considered in modern implosion designs on OMEGA.

This paper presents dual-channel XRTS as a possible diagnostic to retrieve spatial information on the in-flight conditions of an ICF implosion. The analysis is performed by constructing synthetic, spatially integrated, spectra using the collision-radiative code SPECT3D [39], including the x-ray scattering simulator [40], which is a post-processor of the 1-D radiation hydrodynamic code LILAC [41].

II. PROPOSED EXPERIMENTAL SETUP

XRTS is a powerful diagnostic tool for determining the conditions in plasmas where the critical density, $n_c = \epsilon_0 m_e \omega^2/e^2$ (where m_e is the mass of an electron, e is the electron charge, ϵ_0 is the electric constant and ω is the frequency of the laser drive), exceeds what can be probed by any optical source. The first consideration for an experimental setup, is the power required for the X-ray probe in order to produce a scattering signal that can be observed above background noise. The total number of photons in the free-free scattering feature, $N_{\rm scatt}$, can be estimated as [18]

$$N_{\rm scatt} = \left(\frac{E_L}{h\nu}\eta_x\right)\left(\frac{\Omega_{\rm plasma}}{4\pi}\eta_{\rm att}\right)\left(\frac{n_e\sigma_{\rm Th}\ell}{(1+\alpha)^2}\right)\,, \quad (2)$$

where E_L is the probe laser energy, η_x is the conversion efficiency from the laser energy into the probe X-rays, $\eta_{\rm att}$ is the attenuation of the probe X-rays through the dense plasma, $\Omega_{\rm plasma}$ is the solid angles subtended by the plasma, n_e is the electron density, α is the scattering parameter, $\sigma_{\rm Th}$ is the Thomson scattering cross-section and ℓ is the path length of the photons through the plasma.

For the plasma conditions investigated here, the scattering fraction, $n_e\sigma_{\rm Th}\ell$, is approximately equal to 10^{-4}, where representative values for the compressed shell have been taken as $n_e \sim 10^{23}\ \rm cm^{-3}$ and $\ell = 75\ \mu\rm m$. This small scattering fraction makes fielding XRTS challenging since the signal can easily be swamped by significant self-emission from the plasma.

A key benefit of fielding XRTS as a plasma diagnostic, is that XRTS can be split into two scattering regimes, the collective and the noncollective, as determined by the scattering parameter,

$$\alpha = \frac{1}{k\lambda_S}\,, \quad (3)$$

where k is the scattering vector, and λ_S is the screening length. In the noncollective regime, the incoming wave 'probes' through the screening sphere and the scattering spectrum therefore reflects the electron velocity distribution. In contrast, the collective scattering regime reflects the collective motion of the electrons. Designing an experiment where both regimes can be recorded can reduce the error on the inferred plasma parameters.

To model the X-ray emissivity, a 1 kJ laser with a 10 ps pulse length and a source diameter of 50 μm was used to produce a Gaussian X-ray source, with a FWHM of 10 eV, 0.5 cm away from the imploding target, taking an estimate of $\eta_x = 0.01\%$ [42]. This backlighter distance is possible due to the development of a fast target positioner (FASTPOS) in cryogenic implosion by Stoeckl *et al.* [43]. The demonstrative scattering geometry is shown in Figure 1. With these laser and plasma parameters, using equation 2, the total number of scattered photons is $\sim 3 \times 10^7$. The forward scattering was collected at $\theta_F = 40°$ and the backward scattering at $\theta_B = 120°$. The details of the two targets chosen for this investigation are shown in Figures 2 and 3 with adiabats of 2.8 and 8.0, respectively.

Two experimental setups are considered for this paper, one with an X-ray probe energy of 2 keV and the other using a 3.5 keV probe. The scattering regime recorded by each detector in each setup is shown in Figure 4. These two probe energies were selected to investigate the effect different laser energies had on the determined plasma parameters whilst keeping one detector in the collective and the other in the noncollective regime. It should be noted that the values for the α parameter shown in the figure are calculated for the densest region in the compressed DT shell, and therefore not representative of the scattering from the ICF capsule as a whole. To determine the scattering signals from each region of the implosion, the fully integrated scattering spectra must be determined.

The plasmon frequency shift for the high adiabat target is $\sim 27\,\rm eV$, which increases to $\sim 30\,\rm eV$ for the low

adiabat target. In order to distinguish this plasmon scattering, a narrow band X-ray probe must be used (FWHM $< 10\,\mathrm{eV}$). To achieve this in an experimental setup, the source must be chosen carefully.

Previous experiments have successfully used a crystal imaging system with a Si He$_\alpha$ line at $\sim 1.865\,\mathrm{keV}$ to radiograph OMEGA cryogenic implosions [44] but the required x-ray fluence may not be enough. Alternatively, Cl K$_\alpha$ at $\sim 2.62\,\mathrm{keV}$ or Cl Ly-α at $\sim 2.96\,\mathrm{keV}$ could be used [45].

An important consideration to make before extrapolating this work to an experimental campaign, is predicting the level of noise on the scattering signal. In the case of a fusion capsule implosion, there is significant self-emission that will be collected over the time gating of the detector. Representative spectra have been produced for this case study as detailed below.

III. OBTAINING SIMULATED SPATIALLY INTEGRATED SPECTRA

The cryogenic DT implosion plasma conditions were calculated using the LILAC code. The LILAC code is a 1-D spherical Lagrangian, radiation-hydrodynamics code [41] that simulates symmetric, laser direct-drive implosions. It includes laser ray-tracing with an inverse bremsstrahlung model that can also account for cross-beam energy transfer [46]. LILAC also includes a nonlocal thermal transport model that uses a simplified Boltzmann equation with a Krook collision term [47], multigroup radiation diffusion, and a first-principles equation-of-state (FPEOS) model [48, 49] and opacity (FPOT) model [50] derived from molecular dynamics methods.

In this work, the focus is on the time when the capsule is at two-thirds compression, $R_{\mathrm{Ablation\,surface}}/R_{\mathrm{Vapor,\,initial}} = 2/3$. The inhomogenity of the plasma results in different scattering signals from different regions of the plasma. The capability to simulate the fully spatially integrated spectra, accounting for opacity and self-emission of the plasma, is paramount to determine, for a given scattering geometry, the dominant scattering features. This provides insightful information to design the experiments.

SPECT3D is a spectroscopy code produced by Prism Computational Sciences which post-processes hydrodynamics code output and simulates high-resolution spectra and images for LTE and non-LTE plasmas in 1-D, 2-D, and 3-D geometries [39]. It computes a variety of diagnostic signatures that can be compared with experimental measurements including: time-resolved and time-integrated spectra, space-resolved spectra and streaked spectra, filtered and monochromatic images, X-ray diode signals. In a SPECT3D simulation, the radiation incident at a detector is computed by solving the radiative transfer equation along a series of lines-of-sight (LOSs) through the plasma grid. At each plasma volume element along a LOS, the frequency-dependent absorption and emissivity of the plasma is calculated. The scattering cross-section is computed using local values of the plasma conditions based on the formalism originally developed in Refs. [51, 52]. Scattered X-ray photons are added to the local source function, allowing SPECT3D to utilize the same algorithms as it uses for plasma self-emission. It is assumed that the radiation from a non-monochromatic, isotropically emitting point-like X-ray source is scattered within each volume element of the SPECT3D spatial grid. The source is specified by its photon-energy-dependent intensity and location in 3-D space. The intensity of the radiation from the source is adjusted for each volume element based on the distance to the source. It includes attenuation due to plasma absorption and the change in the solid angle. The radiation flux at each pixel in the detector plane is calculated by integrating the scattered radiation along each LOS. The scattering angle is computed for each volume element based on the LOS and the line that connects the volume element center and the source [40].

For this paper, an additional feature was added to the original implementation which allows for certain plasma cells to be excluded from contributing to the scattered signal. This allows for studying the contribution of particular plasma regions to the total scattered spectrum. Models for computing self-emission and absorption coefficients remain the same in each zone regardless of whether the flag for excluding scattered signal is set or not.

The addition of this feature allows spectra from isolated regions of the plasma to be compared to the fully integrated spectra in Figures 2 and 3. The overall spectral shape in each detector is dominated by the scattering from the compressed DT shell due to its high density compared to the hot CH plasma. This gives us confidence that an experiment designed to retrieve scattering spectra at this time during the implosion will be representative of the conditions in the compressed shell.

The spectra in Figure 5 demonstrate the relative strength of the scattering signal to the continuum emission over the time scale of the x-ray laser pulse. The number of detected photons in the free-free scattering feature is calculated as [53],

$$N_{\mathrm{d}} = N_{\mathrm{scatt}} \times \left(\frac{\Omega_{\mathrm{det}}}{4\pi} R_{\mathrm{crystal}} \eta_d \right) = N_{\mathrm{scatt}} \times \Gamma_{\mathrm{det}}\,, \quad (4)$$

where Γ_{det} is the fraction of detected photons determined by Ω_{det}, R_{crystal} and η_d which are the solid angle of the detector, the reflectivity of the crystal and the detector efficiency, respectively. For this case study, a $\Gamma_{\mathrm{det}} \sim 10^{-5}$ is assumed which gives $N_{\mathrm{d}} \sim 300$ to produce a signal capable of resolving the adiabats. This assumption gives approximately 3 photons/eV contributing to the inelastic feature, as shown in Figure 5. Taking a spectral resolution of 3 eV/bin gives ~ 9 photons/bin. With currently available spectrometers, such as ZSPEC at the OMEGA laser facility [54], we can readily achieve $\Gamma_{\mathrm{det}} \sim 10^{-6}$. While this would produce a signal which is only marginally measurable, increasing the fraction of

detected photons could be realized, for example, with a modified design consisting of a disposable x-ray crystal placed much closer to the imploding capsule, or employing new generation of detectors with higher quantum efficiency.

Synthetic experimental noise was added by removing the uniform background signal from the spectra, assuming a logarithmic fit, and using Poisson statistics which estimates the noise as $\sim 1/\sqrt{N_t}$ where N_t is the number of photons per spectral resolution element. The resultant spectra are shown in Figure 6.

Utilizing XRTS to determine the adiabat of an ICF capsule would be a valuable diagnostic development. Figure 6 demonstrates that for experimental conditions with identical scattering setups, the two extreme adiabat conditions considered here produce notably differing scattering spectra. In both the 2 keV and 3.5 keV case, the plasmon scattering seen in the forward scattering detector, can be used to determine the difference in electron density between the two adiabats. The difference between the inelastic scattering features from the two adiabats seen in Figure 6**(c)** is a result of only the low adiabat remaining in the collective scattering regime. The high adiabat's inelastic scattering feature has become dominated by Compton scattering. This is evidenced by the broadening of the inelastic peak and the lose of a forward plasmon shift peak. This change in scattering features is evidence of its higher electron temperature and lower density.

IV. RESULTS

Before extracting the plasma parameters from the spatially integrated simulated spectra, the inverse problem instability must first be addressed, which implies that the same measured spectra could be fitted equally well by very different plasma parameters [55]. Bayesian inference, using Markov-Chain Monte Carlo (MCMC) to sample the multidimensional space, is a more robust approach to explore the behavior of the complex multiparameter simulations [56].

An MCMC exploration fit the entire spectra, assuming two weighted uniform plasma regions, one containing DT and the other CH. Whilst it must be acknowledged that the plasma, as demonstrated above, is not uniform, when performing the MCMC analysis, it is impractical to fit multiple plasma regions to the plasma. This is because to implement this, the searched parameter space for each region would need to be restricted to prevent it from overlapping with others. This would ruin the inherently unbiased analysis performed here. Part of this feasibility research involved resolving how and if the resultant parameters from the homogeneous material regions would be representative of the complex simulation.

The exploration was setup to walk through defined parameter spaces to find the ionization, temperature and density that best fit the forward and backward scattering spectra individually is presented in this paper. The parameter space assumed a uniform distribution with linear sampling for the electron temperature, $1 \leq T_e(\mathrm{eV}) \leq 10^3$, and ionization, $0 \leq Z \leq 1$, whilst taking a logarithmic sampling for the electron density, $10^{20} \leq n_e(\mathrm{cm}^{-3}) \leq 5\times10^{24}$. A large sampling space was used so no bias was placed on the resultant parameters.

The MCMC code works by calculating the likelihood of finding a specific set of parameters, Θ, given the synthetic experimental spectrum, I_{raw}, at each step using Bayesian inference,

$$P(\Theta|I_{\mathrm{raw}}) = \frac{P(I_{\mathrm{raw}}|\Theta)P(\Theta)}{P(I_{\mathrm{raw}})}\,, \tag{5}$$

where $P(\Theta)$ is the prior distribution of possible parameters, $P(I_{\mathrm{raw}})$ is the marginal likelihood of the observed data over all possible parameters and $P(I_{\mathrm{raw}}|\Theta)$ is the likelihood of finding I_{raw} given the input parameters, Θ. The forward model likelihood, $P(I_{\mathrm{raw}}|\Theta) = e^{-\beta_{\mathrm{cost}}}$, is a user defined function that gives an acceptance percentage for each Θ, thus allowing convergence to be found on a parameter space that falls within the experimental noise.

The cost function used to determine the appropriateness of each MCMC spectra calculates the maximum percentage error, to allow equal weighting of the fitting to the elastic and inelastic peaks, between the MCMC spectrum, I_{fit}, and the synthetic experimental spectrum, I_{raw},

$$\beta_{\mathrm{cost}} = \max\left(\frac{I_{\mathrm{fit}} - I_{\mathrm{raw}}}{I_{\mathrm{raw}}}\frac{1}{\sqrt{2}\sigma}\right)^2, \tag{6}$$

where σ is the standard deviation representative of the noise of the synthetic scattering spectra. In an actual experiment the value of σ is not known *a priori* and it must be chosen for MCMC to be able to explore a sufficiently wide parameter space. For this analysis, $\sigma = 0.075$ which produces a range of accepted MCMC fits as shown in Figure 7. The σ is selected such that the noise of the scattering signal falls comfortably within the spread of the accepted fits. Whilst using a cost function such as the sum of squares would produce an overall tighter fit to the spectra, this method assumes a perfect fitting model which can lead to high confidence in false results [55].

To analyze the MCMC data, the DT parameters were plotted on a combined matrix shown in Figure 8. The scatter plots for each scattering angle are shown separately and have been colored to represent the spatial density of points. In Figure 8, the histograms along the diagonal are the combined histograms for both the forward and backward scattering parameters. The mean and standard deviation on each parameter was calculated by fitting a normal distribution to the histograms.

The MCMC parameters were compared to the mass-weighted parameters from the 1-D LILAC simulations. The mass-weighted simulation values were calculated using

$$\langle \mathrm{F} \rangle = \frac{\sum F_i \rho_i 4\pi r_i^2 \mathrm{d}r_i}{\sum \rho_i 4\pi r_i^2 \mathrm{d}r_i}\,, \tag{7}$$

TABLE I. The full spectral analysis MCMC DT fitting parameters, as shown in Figures 7 and 8, compared to the mass-weighted parameters from the LILAC 1D simulations, focused on the compressed DT shell, for each adiabat and each probe.

DT Parameter	$\mathbf{T_e}$ (eV)	$\mathbf{n_e}$ (cm^{-3})	**Z**
Adiabat 2.8			
Simulation	25	5.5×10^{23}	0.97
MCMC 2 keV	33 ± 8	$(5.2 \pm 0.6) \times 10^{23}$	0.94 ± 0.03
MCMC 3.5 keV	25 ± 3	$(5.0 \pm 0.3) \times 10^{23}$	0.95 ± 0.03
Adiabat 8.0			
Simulation	38	3.7×10^{23}	0.97
MCMC 2 keV	50 ± 6	$(2.6 \pm 0.4) \times 10^{23}$	0.88 ± 0.07
MCMC 3.5 keV	56 ± 6	$(3.2 \pm 0.5) \times 10^{23}$	0.87 ± 0.05

where F_i is the desired parameter in zone i. The mass-weighted parameters were determined for each region of the implosion. It can be seen in Table I that the MCMC values are in close agreement with the mass-weighted parameters from the compressed DT shell. As discussed previously, this was an expected result, as the high density in the compressed shell meant it dominated the inelastic scattering features.

V. DISCUSSION

There is good agreement between the mass-averaged simulation parameter values and the MCMC distributions. This was the predicted result, as the high density and relative homogeneity of the compressed DT shell region, dominates the spectrum. The forward scattering fits tend to converge around lower densities, higher temperatures and broader ionizations. This results in either broader or slightly skewed distributions on the DT parameters. This differing numerical convergence occurs because the ratio between the source photon energy FWHM and the width of the inelastic scattering feature in the forward scattering case is very small, particularly for the 2 keV probe. It would therefore be possible to obtain information on the compressed DT conditions solely using a backward scattering detector. In particular, it should be noted that, as can be seen from the parameter density maps in Figure 8, analysis focusing solely on the backward scattering spectra would result in significantly better fits to the electron temperature. In order to improve the fit in the forward scattering regime, either a narrower bandwidth or a higher energy source should be used.

Information obtained regarding the CH plasma is predictably very little. This is due to its lower density compared to the DT compressed shell, meaning it does not contribute to the overall shape of the scattering feature as discussed previously. This therefore means that the weighting of the CH plasma in the MCMC analysis becomes very small and convergence around representative conditions doesn't occur.

Overall, the optimum analysis presented in this paper to resolve the plasma conditions in the compressed shell, using a realistic laser probe from OMEGA EP, is performing MCMC analysis from spectra produced using a backward fielding detector. Using this methodology, the overarching goal of resolving the high and low adiabat implosion conditions was achieved. As the collective forward scattering detector is not required for sufficient convergence on the DT compressed shell parameters, either a 2 keV, 3.5 keV or higher energy x-ray photon energy probe could be used. Better agreement may be achieved between the MCMC parameters and the simulations if a narrower bandwidth (< 10 eV) probe beam could be used, meaning the forward scattering inelastic signal would be more sensitive to the electron density. In fact, this is what would be feasible with a Free Electron Laser [57].

In the future, similar analysis will be performed on the conditions at stagnation, the effect of mixing in the implosion as well as investigations into 2-D and 3-D simulations using DRACO [58] and ASTER [59]. In addition, research and development on a spectrometer to optimize the detection of the XRTS signal is required to meet the constraints shown in this paper.

VI. CONCLUSIONS

In summary, spatially-integrated XRTS spectra for 1-D LILAC simulated conditions of low- and high-adiabat, DT cryogenic implosions have been calculated at two-thirds convergence. Markov-Chain Monte Carlo analysis was performed for two different scattering setups. Information on the compressed shell conditions was obtained as it has been shown to be possible to use the spectral resolution in a spatially integrated measurement to discriminate between different regions in the plasma. Fielding just one detector in the noncollective scattering regime produces good agreement with the compressed shell mass-averaged parameters from the simulation. This technique can be used to resolve both the low- and high-adiabat implosions.

VII. ACKNOWLEDGEMENTS

This material is based upon work supported by the Department of Energy National Nuclear Security Administration under Award Number DE-NA0003856, the University of Rochester, and the New York State Energy Research and Development Authority.

This report was prepared as an account of work sponsored by an agency of the U.S. Government. Neither the U.S. Government nor any agency thereof, nor any of

their employees, makes any warranty, express or implied, or assumes any legal liability or responsibility for the accuracy, completeness, or usefulness of any information, apparatus, product, or process disclosed, or represents that its use would not infringe privately owned rights. Reference herein to any specific commercial product, process, or service by trade name, trademark, manufacturer, or otherwise does not necessarily constitute or imply its endorsement, recommendation, or favoring by the U.S. Government or any agency thereof. The views and opinions of authors expressed herein do not necessarily state or reflect those of the U.S. Government or any agency thereof.

M.F.K. and S.M.V. acknowledge support from the UK EPSRC grant EP/P015794/1 and the Royal Society. S.M.V. is a Royal Society University Research Fellow.

The authors would also like to acknowledge the unnamed reviewer for providing insightful comments and suggestions to strengthen this manuscript.

VIII. AIP PUBLISHING DATA SHARING POLICY

The data that supports the findings of this study are available from the corresponding author, H.P., upon reasonable request.

[1] J. D. Lindl, P. Amendt, R. L. Berger, S. G. Glendinning, S. H. Glenzer, S. W. Haan, R. L. Kauffman, O. L. Landen, and L. J. Suter, Phys. Plasmas **11**, 339 (2004).

[2] O. A. Hurricane, D. A. Callahan, D. T. Casey, P. M. Celliers, C. Cerjan, E. L. Dewald, T. R. Dittrich, T. Döppner, D. E. Hinkel, L. F. B. Hopkins, J. L. Kline, S. L. Pape, T. Ma, A. G. MacPhee, J. L. Milovich, A. Pak, H.-S. Park, P. K. Patel, B. A. Remington, J. D. Salmonson, and P. T. S. . R. Tommasini, Nature **506**, 343 (2014).

[3] S. P. Regan, V. N. Goncharov, T. C. Sangster, E. M. Campbell, R. Betti, J. W. Bates, K. Bauer, T. Bernat, S. Bhandarkar, T. R. Boehly, M. J. Bonino, A. Bose, D. Cao, L. Carlson, R. Chapman, T. Chapman, G. W. Collins, T. J. B. Collins, R. S. Craxton, J. A. Delettrez, D. H. Edgell, R. Epstein, M. Farrell, C. J. Forrest, R. K. Follett, J. A. Frenje, D. H. Froula, M. G. Johnson, C. R. Gibson, L. Gonzalez, C. Goyon, V. Y. Glebov, V. Gopalaswamy, A. Greenwood, D. R. Harding, M. Hohenberger, S. X. Hu, H. Huang, J. Hund, I. V. Igumenshchev, D. W. Jacobs-Perkins, R. T. Janezic, M. Karasik, J. H. Kelly, T. J. Kessler, J. P. Knauer, T. Z. Kosc, R. Luo, S. J. Loucks, J. A. Marozas, F. J. Marshall, M. Mauldin, R. L. McCrory, P. W. McKenty, D. T. Michel, P. Michel, J. D. Moody, J. F. Myatt, A. Nikroo, P. M. Nilson, S. P. Obenschain, J. P. Palastro, J. Peebles, R. D. Petrasso, N. Petta, P. B. Radha, J. E. Ralph, M. J. Rosenberg, S. Sampat, A. J. Schmitt, M. J. Schmitt, M. Schoff, W. Seka, R. Shah, J. R. Rygg, J. G. Shaw, R. Short, W. T. Shmayda, M. J. Shoup, A. Shvydky, A. A. Solodov, C. Sorce, M. Stadermann, C. Stoeckl, W. Sweet, C. Taylor, R. Taylor, W. Theobald, D. P. Turnbull, J. Ulreich, M. D. Wittman, K. M. Woo, K. Youngblood, , and J. D. Zuegel, Nucl. Fusion **59**, 3 (2018).

[4] V. N. Goncharov, S. P. Regan, E. M. Campbell, T. C. Sangster, P. B. Radha, J. F. Myatt, D. H. Froula, R. Betti, T. R. Boehly, J. A. Delettrez, D. H. Edgell, R. Epstein, C. J. Forrest, V. Y. Glebov, D. R. Harding, S. X. Hu, I. V. Igumenshchev, F. J. Marshall, R. L. McCrory, D. T. Michel, W. Seka, A. Shvydky, C. Stoeckl, W. Theobald, , and M. Gatu-Johnson, Nucl. Fusion **59**, 014008 (2017).

[5] E. M. Campbell, V. N. Goncharov, T. C. Sangster, S. P. Regan, P. B. Radha, R. Betti, J. F. Myatt, D. H. Froula, M. J. Rosenberg, I. V. Igumenshchev, W. Seka, A. A. Solodov, A. V. Maximov, J. A. Marozas, T. J. B. Collins, D. Turnbull, F. J. Marshall, A. Shvydky, J. P. Knauer, R. L. McCrory, A. B. Sefkow, M. Hohenberger, P. A. Michel, T. Chapman, L. Masse, C. Goyon, S. Ross, J. W. Bates, M. Karasik, J. Oh, J. Weaver, A. J. Schmitt, K. Obenschain, S. P. Obenschain, S. Reyes, and B. V. Wonterghem, Nucl. Fusion **2**, 37 (2017).

[6] J. A. Gaffney, S. X. Hu, P. Arnault, A. Becker, L. X. Benedict, T. R. Boehly, P. M. Celliers, D. M. Ceperley, O. Čertík, J. Clérouin, G. W. Collins, L. A. Collins, J.-F. Danel, N. Desbiens, M. W. C. Dharmawardana, Y. H. Ding, A. Fernandez-Pañella, M. C. Gregor, P. E. Grabowski, S. Hamel, S. B. Hansen, L. Harbour, X. T. He, D. D. Johnson, W. Kang, V. V. Karasiev, L. Kazandjian, M. D. Knudson, T. Ogitsu, C. Pierleoni, R. Piron, R. Redmer, G. Robert, D. Saumon, A. Shamp, T. Sjostrom, A. V. Smirnov, C. E. Starrett, P. A. Sterne, A. Wardlow, H. D. Whitley, B. Wilson, P. Zhang, and E. Zurek, High Energy Density Phys. **28**, 7 (2018).

[7] S. X. Hu, B. Militzer, V. N. Goncharov, and S. Skupsky, Phys. Rev. Lett. **104**, 235003 (2010).

[8] S. X. Hu, L. A. Collins, T. R. Boehly, Y. H. Ding, P. B. Radha, V. N. Goncharov, V. V. Karasiev, G. W. Collins, S. P. Regan, and E. M. Campbell, Phys. Plasmas **25**, 056306 (2018).

[9] S. X. Hu, Phys. Rev. Lett. **119**, 065001 (2017).

[10] C. Wang, Y. Long, X. He, J.-F. Wu, W.-H. Ye, and P. Zhang, Phys. Rev. E **88**, 013106 (2013).

[11] S. M. Vinko, O. Ciricosta, and J. S. Wark, Nature Comms. **5**, 3533 (2013).

[12] D. A. Chapman, J. Vorberger, L. B. Fletcher, R. A. Baggott, L. Divol, T. Döppner, R. W. Falcone, S. H. Glenzer, G. Gregori, T. M. Guymer, A. L. Kritcher, O. L. Landen, T. Ma, A. E. Pak, and D. O. Gericke, Nature Comms. **6**, 6839 (2015).

[13] T. G. White, N. J. Hartley, B. Borm, B. J. B. Crowley, J. W. O. Harris, D. C. Hochhaus, T. Kaempfer, K. Li, P. Neumayer, L. K. Pattison, F. Pfeifer, S. Richardson, A. P. L. Robinson, I. Uschmann, , and G. Gregori, Phys. Rev. Lett. **112**, 145005 (2014).

[14] P. Grabowski, S. Hansen, M. Murillo, L. Stanton, F. Graziani, A. Zylstra, S. Baalrud, P. Arnault, A. Baczewski, L. Benedict, C. Blancard, O. Čertík, J. Clérouin, L. Collins, S. Copeland, A. Correa, J. Dai, J. Daligault, M. Desjarlais, M. Dharma-wardana, G. Faussurier, J. Haack, T. Haxhimali, A. Hayes-Sterbenz, Y. Hou, S. Hu, D. Jensen, G. Jungman, G. Kagan, D. Kang, J. Kress, Q. Ma, M. Marciante, E. Meyer, R. Rudd, D. Saumon, L. Shulenburger, R. Singleton, T. Sjostrom, L. Stanek, C. Starrett, C. Ticknor, S. Valaitis, J. Venzke, and A. White, High Energy Density Physics **37**, 100905 (2020).

[15] O. A. Hurricane, P. T. Springer, P. K. Patel, D. A. Callahan, K. Baker, D. T. Casey, L. Divol1, T. Döppner, D. E. Hinkel, M. Hohenberger, L. F. B. Hopkins, C. Jarrott, A. Kritcher, S. L. Pape, S. Maclaren, L. Masse, A. Pak, J. Ralph, C. Thomas, P. Volegov, , and A. Zylstra, Phys. Plasmas **26**, 052704 (2019).

[16] V. Y. Glebov, T. C. Sangster, C. Stoeckl, J. P. Knauer, W. Theobald, K. L. Marshall, M. J. S. III, T. Buczek, M. Cruz, T. Duffy, M. Romanofsky, M. Fox, A. Pruyne, M. J. Moran, R. A. Lerche, J. McNaney, J. D. Kilkenny, M. J. Eckart, D. Schneider, D. Munro, W. Stoeffl, R. Zacharias, J. J. Haslam, T. Clancy, M. Yeoman, D. Warwas, C. J. Horsfield, J.-L. Bourgade, O. Landoas, L. Disdier, G. A. Chandler, , and R. J. Leeper, Rev. Sci. Instrum. **81**, 10D325 (2010).

[17] S. P. Regan, K. Falk, G. Gregori, P. B. Radha, S. X. Hu, T. R. Boehly, B. J. B. Crowley, S. H. Glenzer, O. L. Landen, D. O. Gericke, T. Döppner, D. D. Meyerhofer, C. D. Murphy, T. C. Sangster, , and J. Vorberger, Phys. Rev. Letters **109**, 265003 (2012).

[18] S. H. Glenzer and R. Redmer, Rev. of Modern Phys. **81**, 1625 (2009).

[19] G. Gregori, S. H. Glenzer, K. B. Fournier, K. M. Campbell, E. L. Dewald, O. S. Jones, J. H. Hammer, S. B. Hansen, R. J. Wallace, , and O. L. Landen, Phys. Rev. Lett. **101**, 045003 (2008).

[20] D. A. Chapman, D. Kraus, A. L. Kritcher, B. Bachmann, G. W. Collins, R. W. Falcone, J. A. Gaffney, D. O. Gericke, S. H. Glenzer, T. M. Guymer, J. A. Hawreliak, O. L. Landen, S. L. Pape, T. Ma, P. Neumayer, J. Nilsen, A. Pak, R. Redmer, D. C. Swift, J. Vorberger, and T. Döppner, Phys. Plasmas **21**, 082709 (2014).

[21] E. J. Gamboa, P. A. Keiter, R. P. Drake, K. Falk, D. S. Montgomery, and J. F. Benage, High Energy Density Physics **11**, 75 (2014).

[22] T. R. Boehly, D. L. Brown, R. S. Craxton, R. L. Keck, J. P. Knauer, J. H. Kelly, T. J. Kessler, S. A. Kumpan, S. J. Loucks, S. A. Letzring, F. J. Marshall, R. L. McCrory, S. F. B. Morse, W. Seka, J. M. Soures, and C. P. Verdon, Optics Communications **133**, 495 (1997).

[23] E. J. Gamboa, C. M. Huntington, M. R. Trantham, P. A. Keiter, R. P. Drake, D. S. Montgomery, J. F. Benage, and S. A. Letzring, Rev. of Sci. Instrum. **83**, 10E108 (2012).

[24] P. Davis, T. Döppner, J. R. Rygg, C. Fortmann, L. Divol, A. Pak, L. Fletcher, A. Becker, B. Holst, P. Sperling, R. Redmer, M. P. Desjarlais, P. Celliers, G. W. Collins, O. L. Landen, R. W. Falcone, and S. H. Glenzer, Nature Comm. **7**, 11189 (2016).

[25] A. K. Kritcher, T. Doeppner, C. Fortmann, T. Ma, O. L. Landen, R. Wallance, and S. H. Glenzer, Phys. Rev. Letters **107**, 015002 (2011).

[26] L. B. Fletcher, A. L. Kritcher, A. Pak, T. Ma, T. Doeppner, C. Fortmann, L. Divol, O. S. Jones, O. L. Landen, H. A. Scott, J. Vorberger, D. A. Chapman, D. O. Gericke, B. A. Mattern, G. T. Seidler, and G. Gregori, Phys. Rev. Letters **112**, 145004 (2014).

[27] J. Lindl, *Inertial Confinement Fusion* (Springer, New York, 1998).

[28] R. S. Craxton, K. S. Anderson, T. R. Boehly, V. N. Goncharov, D. R. Harding, J. P. Knauer, R. L. McCrory, P. W. McKenty, D. D. Meyerhofer, J. F. Myatt, A. J. Schmitt, J. D. Sethian, R. W. Short, S. Skupsky, W. Theobald, W. L. Kruer, K. Tanaka, R. Betti, T. J. B. Collins, J. A. Delettrez, S. X. Hu, J. A. Marozas, A. V. Maximov, D. T. Michel, P. B. Radha, S. P. Regan, T. C. Sangster, W. Seka, A. A. Solodov, J. M. Soures, C. Stoeckl, and J. D. Zuegel, Phys. Plasmas **22**, 110501 (2015).

[29] R. Betti and O. Hurricane, Nature Phys. **12**, 435 (2016).

[30] S. Atzeni and J. Meyer-Ter-Vehn, *The Physics of Inertial Fusion* (Oxford University Press, 2004).

[31] O. L. Landen, D. T. Casey, J. M. DiNicola, T. Doeppner, E. P. Hartouni, D. E. Hinkel, L. F. B. Hopkins, M. Hohenberger, A. L. Kritcher, S. L. Pape, B. J. MacGowan, S. Maclaren, K. D. Meaney, M. Millot, P. K. Patel, J. Park, L. A. Pickworth, H. F. Robey, J. S. Ross, S. T. Yang, A. B. Zylstra, K. L. Baker, D. A. Callahan, P. M. Celliers, M. J. Edwards, O. A. Hurricane, J. D. Lindl, J. D. Moody, J. Ralph, V. A. Smalyuk, C. A. Thomas, B. M. V. Wonterghem, and C. R. Weber, High Energy Density Phys. **36**, 100755 (2020).

[32] M. J. Edwards, P. K. Patel, J. D. Lindl, L. J. Atherton, S. H. Glenzer, S. W. Haan, J. D. Kilkenny, O. L. Landen, E. I. Moses, A. Nikroo, R. Petrasso, T. C. Sangster, P. T. Springer, S. Batha, R. Benedetti, L. Bernstein, R. Betti, D. L. Bleuel, T. R. Boehly, D. K. Bradley, J. A. Caggiano, D. A. Callahan, P. M. Celliers, C. J. Cerjan, K. C. Chen, D. S. Clark, G. W. Collins, E. L. Dewald, L. Divol, S. Dixit, T. Doeppner, D. H. Edgell, J. E. Fair, M. Farrell, R. J. Fortner, J. Frenje, M. G. G. Johnson, E. Giraldez, V. Y. Glebov, G. Grim, B. A. Hammel, A. V. Hamza, D. R. Harding, S. P. Hatchett, N. Hein, H. W. Herrmann, D. Hicks, D. E. Hinkel, M. Hoppe, W. W. Hsing, N. Izumi, B. Jacoby, O. S. Jones, D. Kalantar, R. Kauffman, J. L. Kline, J. P. Knauer, J. A. Koch, B. J. Kozioziemski, G. Kyrala, K. N. LaFortune, S. L. Pape, R. J. Leeper6, R. Lerche, T. Ma, B. J. MacGowan, A. J. MacKinnon, A. Macphee, E. R. Mapoles, M. M. Marinak, M. Mauldin, P. W. McKenty, M. Meezan, P. A. Michel, J. Milovich, J. D. Moody, M. Moran, D. H. Munro, C. L. Olson6, K. Opachich, A. E. Pak, T. Parham, H.-S. Park, J. E. Ralph, S. P. Regan, B. Remington, H. Rinderknecht, H. F. Robey, M. Rosen, S. Ross, J. D. Salmonson, J. Sater, D. H. Schneider, F. H. Séguin, S. M. Sepke, D. A. Shaughnessy, V. A. Smalyuk, B. K. Spears, C. Stoeckl, W. Stoeffl, L. Suter, C. A. Thomas, R. Tommasini, R. P. Town, S. V. Weber, P. J. Wegner, K. Widman, M. Wilke, D. C. Wilson, C. B. Yeamans, , and A. Zylstra3, Phys. Plasmas **20**, 070501 (2013).

[33] K. Anderson and R. Betti, Phys. Plasmas **11**, 5 (2004).

[34] J. Melvin, H. Lim, V. Rana, B. Cheng, J. Glimm, D. H. Sharp, and D. C. Wilson, Phys. Plasmas **22**, 022708 (2015).

[35] T. R. Dittrich, O. A. Hurricane, D. A. Callahan, E. L. Dewald, T. Döppner, D. E. Hinkel, L. F. B. Hopkins,

S. L. Pape, T. Ma, J. L. Milovich, J. C. Moreno, P. K. Patel, H.-S. Park, B. A. Remington, J. D. Salmonson, , and J. L. Kline, Phys. Rev. Letters **112**, 055002 (2014).

[36] C. Cerjan, P. T. Springer, and S. M. Sepke, Phys. Plasmas **20**, 056319 (2013).

[37] V. Gopalaswamy, R. Betti, J. P. Knauer, N. Luciani, D. Patel, K. M. Woo, A. Bose, I. V. Igumenshchev, E. M. Campbell, K. S. Anderson, K. A. Bauer, M. J. Bonino, D. Cao, A. R. Christopherson, G. W. Collins, T. J. B. Collins, J. R. Davies, J. A. Delettrez, D. H. Edgell, R. Epstein, C. J. Forrest, D. H. Froula, V. Y. Glebov, V. N. Goncharov, D. R. Harding, S. X. Hu, D. W. Jacobs-Perkins, R. T. Janezic, J. H. Kelly, O. M. Mannion, A. Maximov, F. J. Marshall, D. T. Michel, S. Miller, S. F. B. Morse, J. Palastro, J. Peebles, P. B. Radha, S. P. Regan, S. Sampat, T. C. Sangster, A. B. Sefkow, W. Seka, R. C. Shah, W. T. Shmyada, A. Shvydky, C. Stoeckl, A. A. Solodov, W. Theobald, J. D. Zuegel, M. G. Johnson, R. D. Petrasso, C. K. Li, and J. A. Frenje, Nature **565**, 581 (2019).

[38] V. N. Goncharov, T. C. Sangster, R. Betti, T. R. Boehly, M. J. Bonino, T. J. B. Collins, R. S. Craxton, J. A. Delettrez, D. H. Edgell, R. Epstein, R. K. Follett, C. J. Forrest, D. H. Froula, V. Y. Glebov, D. R. Harding, R. J. Henchen, S. X. Hu, I. V. Igumenshchev, R. Janezic, J. H. Kelly, T. J. Kessler, T. Z. Kosc, S. J. Loucks, J. A. Marozas, F. J. Marshall, A. V. Maximov, R. L. McCrory, P. W. McKenty, D. D. Meyerhofer, D. T. Michel, J. F. Myatt, R. Nora, P. B. Radha, S. P. Regan, W. Seka, W. T. Shmayda, R. W. Short, A. Shvydky, S. Skupsky, C. Stoeckl, B. Yaakobi, J. A. Frenje, M. Gatu-Johnson, R. D. Petrasso, and D. T. Casey, Phys. Plasmas **21**, 056315 (2014).

[39] J. J. MacFarlane, I. Golovkin, P. Wang, P. R. Woodruff, and N. A. Pereyra, High Energy Density Phys. **3**, 181 (2007).

[40] I. Golovkin, J. J. MacFarlane, P. Woodruff, I. Hall, G. Gregori, J. Bailey, E. Harding, T. Ao, and S. Glenzer, High Energy Density Phys. **9**, 510 (2013).

[41] J. Delettrez, R. Epstein, M. Richardson, P. A. Jaanimagi, and B. L. Henke, Phys. Rev. A **36**, 3926 (1987).

[42] C. Stoeckl, M. Bonino, C. Mileham, S. Regan, W. Theobald, T. Ebert, and S. Sander, High Energy Density Phys. **41**, 100973 (2021).

[43] C. Stoeckl, M. Bedzyk, G. Brent, R. Epstein, G. Fiksel, D. Guy, V. N. Goncharov, S. X. Hu, S. Ingraham, D. W. Jacobs-Perkins, R. K. Jungquist, F. J. Marshall, C. Mileham, P. M. Nilson, T. C. Sangster, M. J. Shoup, and W. Theobald, Rev. Sci. Instrum. **85**, 11E501 (2014).

[44] C. Stoeckl, R. Epstein, R. Betti, W. Bittle, J. A. Delettrez, C. J. Forrest, V. Y. Glebov, V. N. Goncharov, D. R. Harding, I. V. Igumenshchev, D. W. Jacobs-Perkins, R. T. Janezic, J. H. Kelly, T. Z. Kosc, R. L. McCrory, D. T. Michel, C. Mileham, P. W. McKenty, F. J. Marshall, S. F. B. Morse, S. P. Regan, P. B. Radha, B. Rice, T. C. Sangster, M. J. Shoup, W. T. Shmayda, C. Sorce, W. Theobald, J. Ulreich, M. D. Wittman, D. D. Meyerhofer, J. A. Frenje, M. G. Johnson, and R. D. Petrasso, Physics of Plasmas **24**, 056304 (2017).

[45] M. K. Urry, G. Gregori, O. L. Landen, A. Pak, and S. H. Glenzer, J. Quant. Spectroscopy and Rad. Transfer **99**, 636 (2006).

[46] I. V. Igumenshchev, D. H. Edgell, V. N. Goncharov, J. A. Delettrez, A. V. Maximov, J. F. Myatt, W. Seka, A. Shvydky, S. Skupsky, and C. Stoeckl, Physics of Plasmas **17**, 122708 (2010).

[47] V. N. Goncharov, O. V. Gotchev, E. Vianello, T. R. Boehly, J. P. Knauer, P. W. McKenty, P. B. Radha, S. P. Regan, T. C. Sangster, S. Skupsky, V. A. Smalyuk, R. Betti, R. L. McCrory, D. D. Meyerhofer, and C. Cherfils-Clérouin, Physics of Plasmas **13**, 012702 (2006).

[48] S. X. Hu, B. Militzer, V. N. Goncharov, and S. Skupsky, Phys. Rev. B **84**, 224109.

[49] S. X. Hu, L. A. Collins, V. N. Goncharov, J. D. Kress, R. L. McCrory, and S. Skupsky, Phys. Rev. E **92**, 043104 (2015).

[50] S. X. Hu, L. A. Collins, V. N. Goncharov, T. R. Boehly, R. Epstein, R. L. McCrory, and S. Skupsky, Phys. Rev. E **90**, 033111 (2014).

[51] G. Gregori, S. H. Glenzer, W. Rozmus, R. W. Lee, and O. L. Landen, Phys. Rev. E **67**, 026412 (2003).

[52] B. J. B. Crowley and G. Gregori, New J. of Phys. **15**, 015014 (2013).

[53] H. Sawada, S. P. Regan, D. D. Meyerhofer, I. V. Igumenshchev, V. N. Goncharov, T. R. Boehly, R. Epstein, T. C. Sangster, V. A. Smalyuk, B. Yaakobi, G. Gregori, S. H. Glenzer, and O. L. Landen, Phys. of Plasmas **14**, 122703 (2007).

[54] A. M. Saunders, A. Jenei, T. Döppner, R. W. Falcone, D. Kraus, A. Kritcher, O. L. Landen, J. Nilsen, and D. Swift, Rev. Sci. Instrum. **87**, 11E724 (2016).

[55] M. Kasim, T. P. Galligan, J. Topp-Mugglestone, G. Gregori, and S. M. Vinko, Phys. Plasmas **26**, 112706 (2019).

[56] C. Andrieu, N. de Freitas, A. Doucet, and M. Jordan, Mach. Learn. **50**, 5 (2003).

[57] L. B. Fletcher, H. J. Lee, T. Döppner, E. Galtier, B. Nagler, P. Heimann, C. Fortmann, S. LePape, T. Ma, M. Millot, A. Pak, D. Turnbull, D. A. Chapman, D. O. Gericke, J. Vorberger, T. White, G. Gregori, M. Wei, B. Barbrel, R. W. Falcone, C.-C. Kao, H. Nuhn, J. Welch, U. Zastrau, P. Neumayer, J. B. Hastings, and S. H. Glenzer, Nature Photonics **9**, 274 (2015).

[58] P. B. Radha, T. J. B. Collins, J. A. Delettrez, Y. Elbaz, R. Epstein, V. Y. Glebov, V. N. Goncharov, R. L. Keck, J. P. Knauer, J. A. Marozas, F. J. Marshall, R. L. McCrory, P. W. McKenty, D. D. Meyerhofer, S. P. Regan, T. C. Sangster, W. Seka, D. Shvarts, S. Skupsky, Y. Srebro, and C. Stoeckl, Phys. Plasmas **12**, 056307 (2005).

[59] I. V. Igumenshchev, V. N. Goncharov, F. J. Marshall, J. P. Knauer, E. M. Campbell, C. J. Forrest, D. H. Froula, V. Y. Glebov, R. L. McCrory, S. P. Regan, T. C. Sangster, S. Skupsky, and C. Stoeckl, Phys. Plasmas **23**, 052702 (2016).

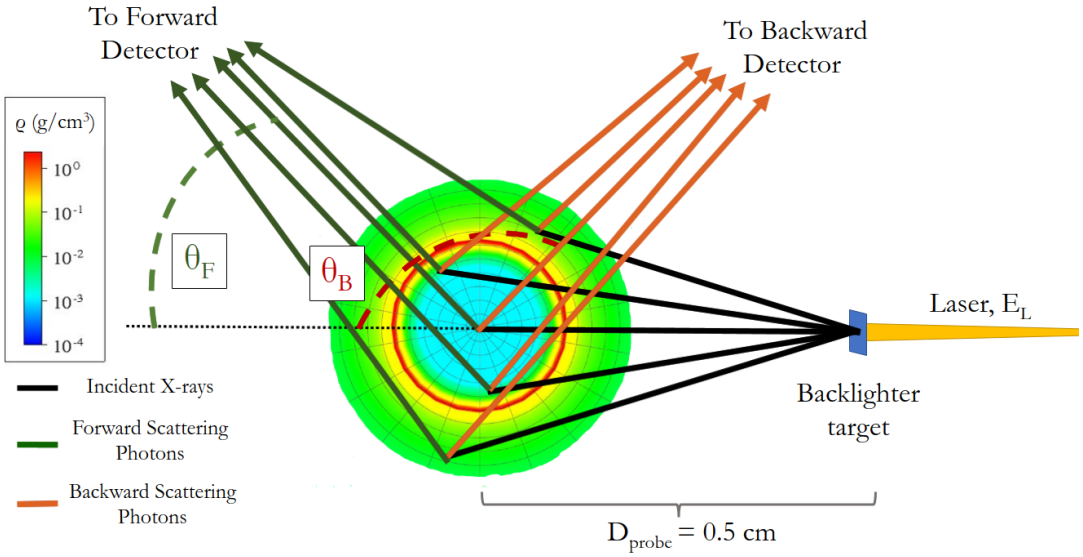

FIG. 1. A sketch of the proposed experimental setup, with a laser of energy E_L incident on a backlighter target, producing X-rays with a conversion efficiency of η_x. The scattering X-rays are shown incident on the 3D inferred density profile from Spect3D using the 1D simulation data produced by the LILAC code. Schematic of the scattering events, recorded on the detector by SPECT3D, from different zones throughout the implosion are shown. The scattering geometry is demonstrative and not drawn to scale.

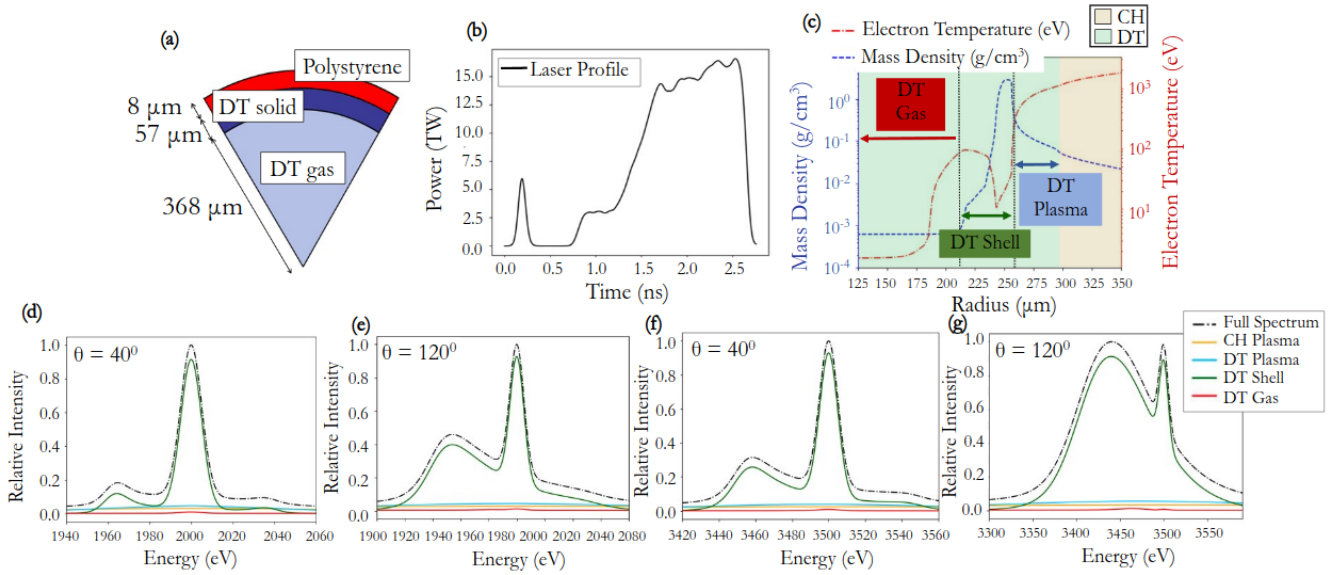

FIG. 2. **(a)** Simulated target design, with an adiabat of 2.8, fired with laser profile shown in **(b)**. **(c)** Density and electron temperature conditions in the ICF implosion across the shock wave (propagating to the left) at two-thirds compression, $t = 2215$ ps, as determined by the LILAC code for the target. The scattering contributions from the DT in the unshocked fuel, compressed shell and coronal plasma has been isolated and compared to the fully integrated spectrum. For a 2 keV probe, the contribution from each region of the plasma to the overall scattering spectrum is shown for both the forward (40°), **(d)**, and backward (120°) scattering regime, **(e)**. The same breakdown of the plasma has been performed with a 3.5 keV energy probe in **(f)** and **(g)**.

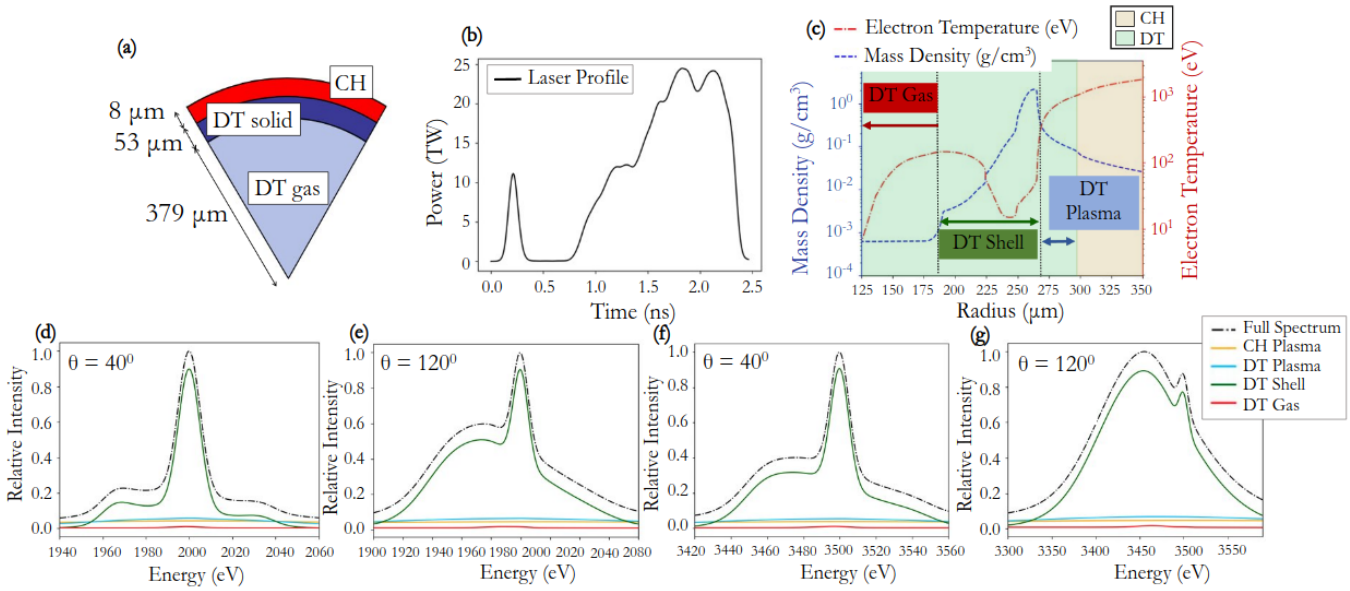

FIG. 3. As with Figure 2 but with an ICF capsule with an adiabat of 8.0 and at $t = 1901$ ps.

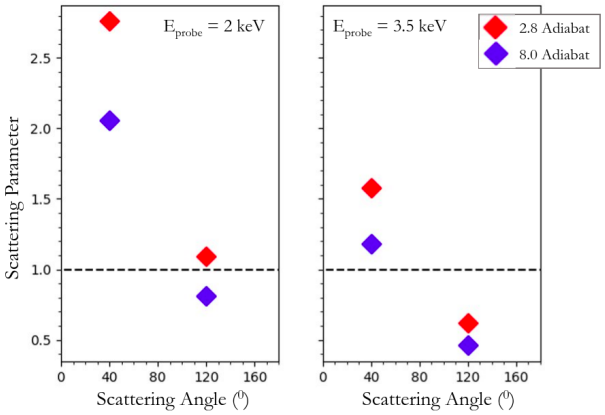

FIG. 4. Scattering parameters, α, as calculated for the densest zone in the compressed DT shell for each adiabat, scattering angle and probe energy. A dashed line is shown at $\alpha = 1$ which is the approximate separation of collective, $\alpha > 1$, and noncollective, $\alpha \leq 1$, scattering.

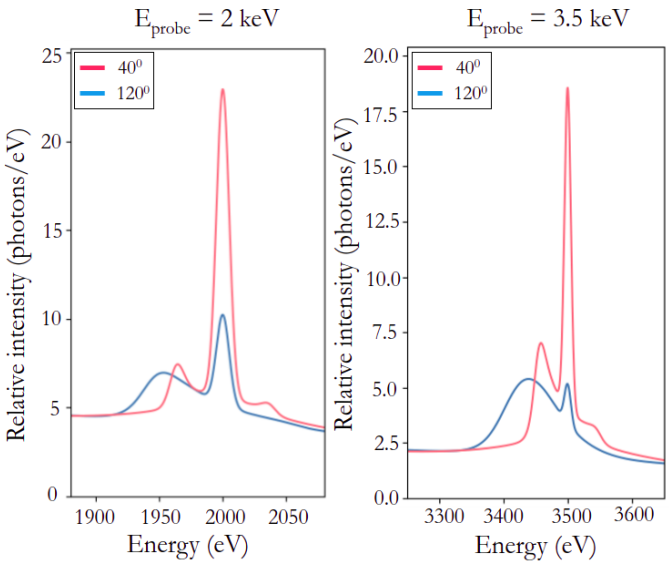

FIG. 5. Total relative detected signal per eV, where $\Gamma_{\rm det}$ is assumed to be 10^{-5}, integrated over the time of the x-ray laser pulse = 10 ps. The signal is shown for the target with an adiabat of 2.8 with both the 2 keV and 3.5 keV laser photon energies.

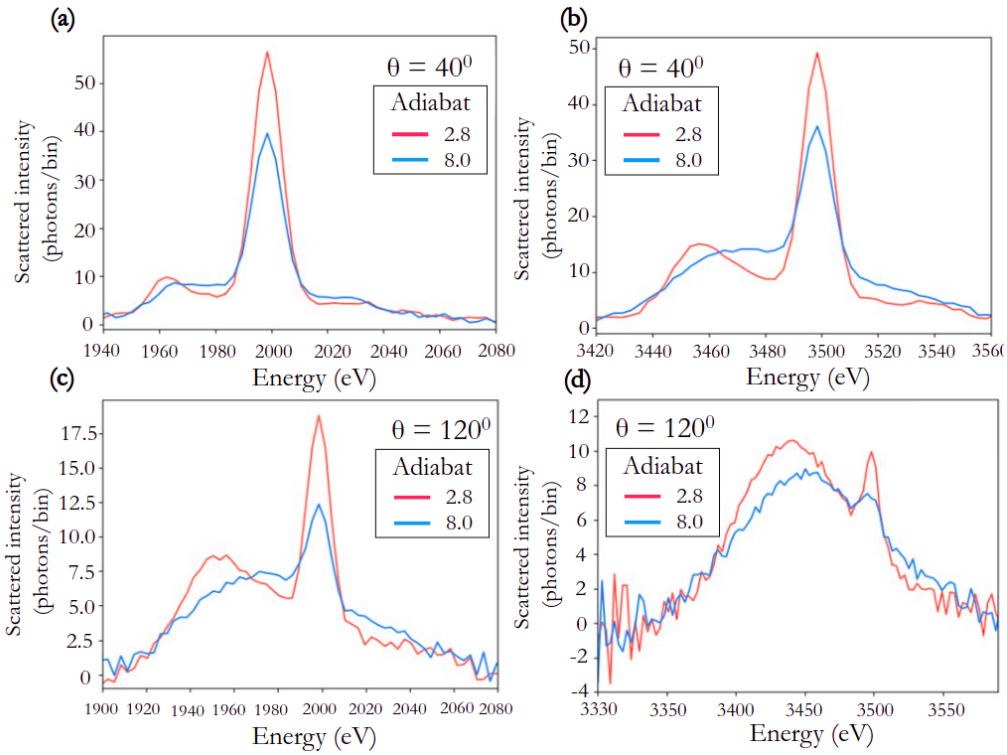

FIG. 6. Synthetic experimental x-ray scattering data produced by Spect3D for LILAC simulations with adiabats of 2.8 and 8.0, assuming 3 eV/bin and Poisson statistics to simulate noise. **(a)** and **(b)** Forward scattering spectra for a 2 keV probe and a 3.5 keV probe, respectively. **(c)** and **(d)** Backward scattering spectra for a 2 keV probe and a 3.5 keV probe, respectively.

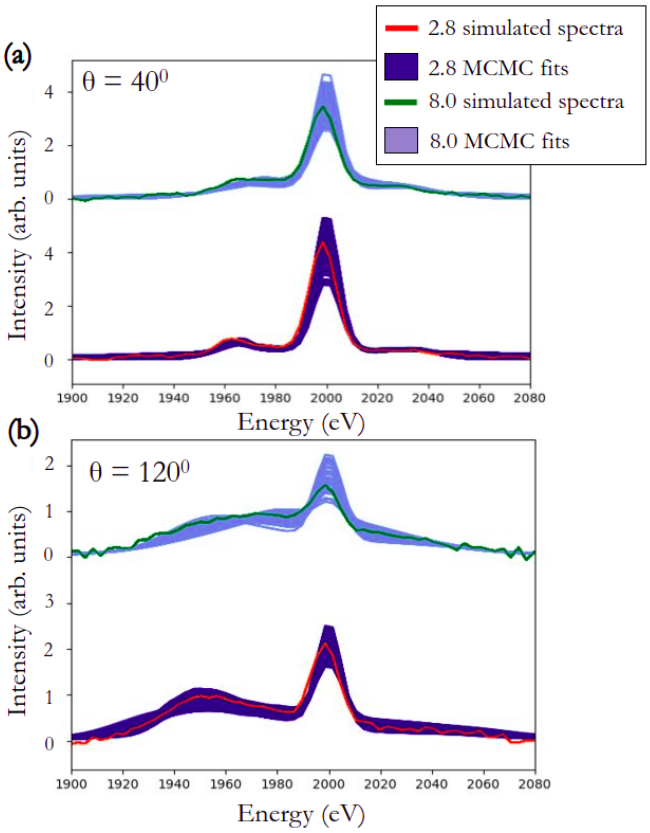

FIG. 7. Accepted MCMC fits using a 2 keV photon energy probe with the **(a)** 40° and **(b)** 120° detectors.

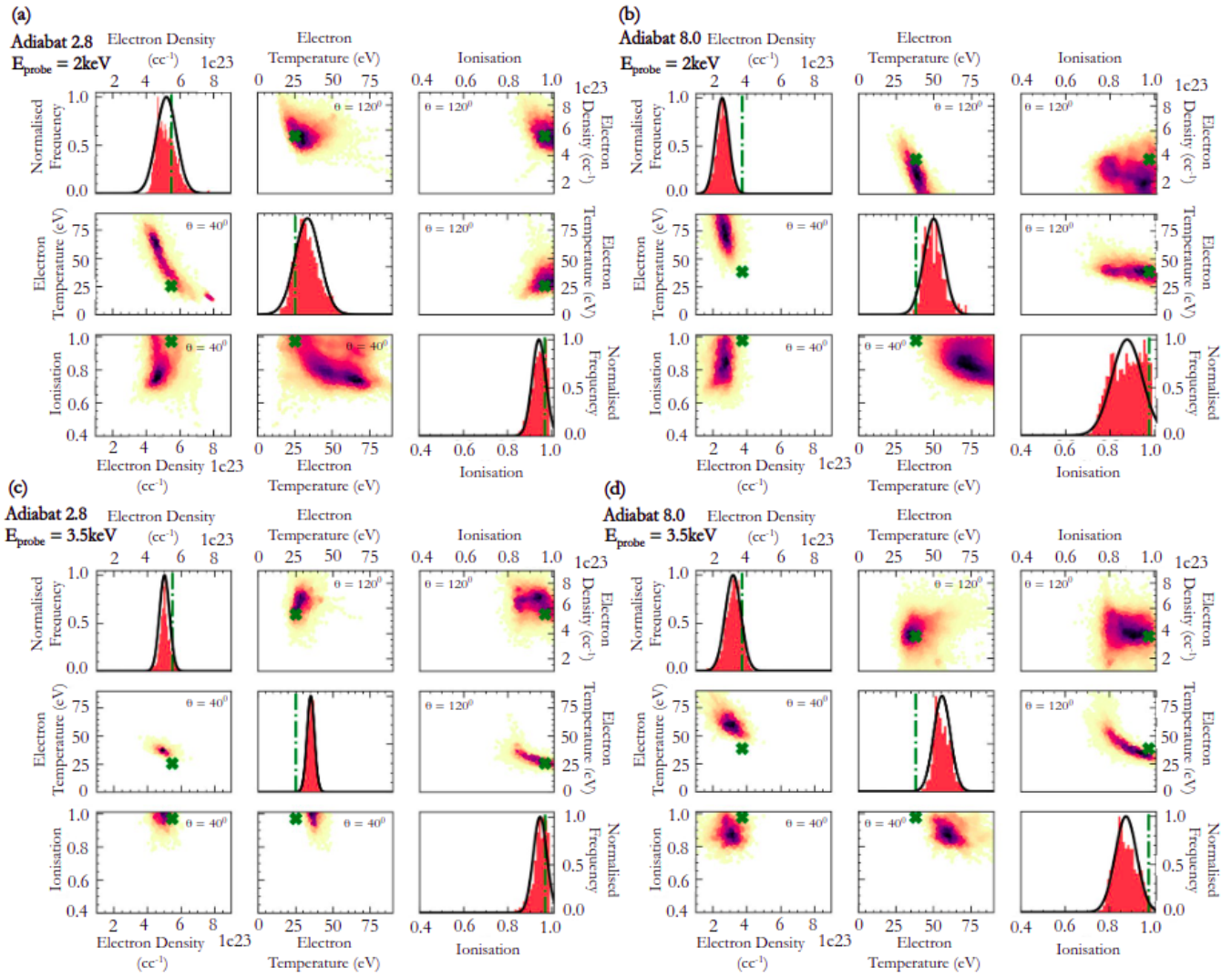

FIG. 8. MCMC parameter convergence fitting the entire spectrum using equation 6 as a cost function. Variation in DT plasma parameters from; **(a)** 2.8 adiabat and 2 keV probe, **(b)** 8.0 adiabat and 2 keV probe, **(c)** 2.8 adiabat and 3.5 keV probe, and **(d)** 8.0 adiabat and 3.5 keV probe. The scatter plots show the correlation between each DT parameter. The lower quadrant scatter plots are taken from the 40° scattering data, whilst the upper quadrant shows the 120° scattering data. The scatter plots have been colored to represent the spatial density of points. The diagonal plots show the combined histograms for each parameter from both the scattering regimes. Superimposed on each histogram is a normal distribution of the fits. The mass-averaged parameter values from the LILAC 1-D simulation are highlighted as a green dashed line or cross.